https://doi.org/10.1016/j.solmat.2018.01.004

Strategies for High Performance Perovskite/Crystalline Silicon Four-Terminal Tandem Solar Cells

Zhiwei Ren[a, 1], Jixiang Zhou[b, e, 1], Yaokang Zhang[c], Annie Ng[a], Qian Shen[a], Sin Hang Cheung[d], Hui Shen, [b, e, *] Kan Li[c], Zijian Zheng[c], Shu Kong So[d], Aleksandra B. Djurišić,[f] Charles Surya[a,*]

[a] Department of Electronic and Information Engineering, The Hong Kong Polytechnic University, Hong Kong, P.R. China

[b] Institute for Solar Energy Systems, Sun Yat-Sen University, Guangzhou, Guangdong Province, P.R. China;

[c]Institute of Textiles and Clothing, The Hong Kong Polytechnic University, Hong Kong, P.R. China

[d]Department of Physics, Hong Kong Baptist University, Hong Kong, P.R. China

[e]ShunDe SYSU Institute for Solar Energy, No. 1, Deshengdong Road, Shunde, Guangdong, PR China

[f]Department of Physics, University of Hong Kong, Hong Kong, P.R. China

[*]Corresponding author: charles.surya@polyu.edu.hk, shenhui1956@163.com

[1]These authors contributed equally to this work.

Keywords: tandem solar cells, perovskites, silicon, transparent electrodes, oxygen annealing, biomimicking elastomeric petals

In this work, we report systematic studies on improving the optical and electrical properties of four-terminal perovskite/c-Si tandem solar cells. Light harvesting power of the device is significantly enhanced due to the complementary absorption spectra of perovskite and c-Si absorber materials. To obtain high power conversion efficiency (PCE) for the device, careful engineering of optoelectronic properties of the devices are accomplished through three effective techniques: 1. Oxygen annealing treatment for reducing defect density of perovskite materials; 2. Optical engineering of the transparent electrode (MoO_3/Au/MoO_3) to obtain high transmission at long wavelengths for the tandem solar cell applications; and 3. Enhancement of

light harvesting power achieved by using the novel biomimicking elastomeric petals as the light trapping layer. The individual perovskite solar cell (PSC) with MoO_3/Au/MoO_3 electrode with or without light trapping layer yields an average PCE of 16.6 % and 16.0 % respectively. By combining c-Si bottom cell with perovskite top cell mechanically, an overall PCE of 22.1 % is achieved for the averaged value, which is a promising result for future development of perovskite based tandem solar cells.

1. Introduction

The development of metal halide perovskite, a low-cost material with a crystal structure of calcium titanate, has recently made tremendous progress towards photovoltaic (PV) applications in terms of efficiency [1, 2] and stability [3-5]. In 2009, Kojima *et al*. [6] reported PV properties of perovskite and utilized it as sensitizers in photoelectrochemical cells, yielding a PCE of 3.8%. The first all solid-state PSC was demonstrated by Kim *et al*. with a PCE of 9.7% [7]. After these pioneer studies, enormous attentions from scientists worldwide have been attracted to the perovskite materials, triggering intensive research on its PV properties and applications. Today, only a few years from its first report, PSCs exhibit skyrocketing enhancements in efficiencies and already reached a certified PCE of 22.1% [8]. The rapid enhancement in the efficiency achieved by PSCs is attributed to the physical properties of perovskite materials such as their broadly tunable bandgaps [9], high absorption coefficients over a wide range of visible light spectrum [10], long carrier diffusion lengths [11-12], good crystallinity [13,14] and high carrier mobilities [14-16]. The desirable properties of the perovskite and the promising results reveal that PSCs have huge potential to compete with the state-of-the-art PV technologies such as copper indium gallium diselenide (CIGS) solar cells and crystalline silicon solar cells (c-Si). It is noteworthy that c-Si solar cells have been dominating the PV market for several decades with relatively marginal enhancement in performance over the past years. The world record PCE for Si-based solar cells is currently at 26.6% [17] achieved by the amorphous silicon/crystalline silicon heterojunction structure,

which is approaching the theoretical limit of 29.4% [18]. Considering the fact that Si solar cells have strong PV response at long wavelengths, combining Si solar cells with other types of solar cells with strong PV response at short wavelengths is an effective strategy to overcome the efficiency bottleneck. High efficiency tandem solar cells have been developed by stacking wide-bandgap compound semiconductor such as gallium arsenide [19] and indium gallium phosphide [20] on top of Si. However, these classes of solar cells are prohibitively costly for commercial terrestrial applications. Perovskite materials with tunable bandgap energies and low fabrication cost are promising candidates for the top cell in tandem with the small bandgap c-Si solar cell. The perovskite/c-Si tandem structure offers an effective approach to broaden the PV response to the solar spectrum and to minimize loss due to thermalization by adopting light absorbers with complementary absorption spectra. Recently, several groups have successfully demonstrated perovskite/Si tandem solar cells in different structures with promising PCEs. Chen *et al.* [21] have reported that using an efficient copper (Cu)/ gold (Au) semitransparent electrode yields a PCE of 16.5 % for individual perovskite top solar cell and a PCE of 23.0% for perovskite/Si tandem solar cells. Bailie *et al* [22]. utilized a transparent silver (Ag) nanowire electrode on PSC to achieve a PCE of 12.7 % for individual perovskite top cell and a PCE of 17.0 % for perovskite/Si tandem solar cells (18.6 % for perovskite/CIGS tandem solar cells). Albrecht *et al.* [24] and Werner *et al*. [24] have demonstrated perovskite/Si tandem solar cell in monolithic structure with the PCE of 18 % and 21.2 % respectively. The high PCE values obtained from different groups clearly indicate the huge potential of using the tandem configuration.

A tandem solar cell is generally designed in three different configurations: monolithic two-terminal tandems with a tunnel junction (recombination layer) [25,26]; monolithic three-terminal tandems with the middle electrode being shared between the two sub cells [27,28] or mechanically stacked four-terminal tandems [29,30]. Several review papers have summarized

and compared different types of perovskite based tandem devices [XX, XX]. In a monolithic two-terminal tandem system, the top cell is directly fabricated on the bottom cell, which allows simplified manufacturing steps and minimizes parasitic absorption due to the transparent conductive oxide (TCO) electrodes such as indium tin oxide (ITO) and fluorine doped tin oxide (FTO). However, the total current of a monolithic two-terminal tandem cell is determined by the lowest of the currents generated in either the top cell or the bottom cell [31]. Therefore, precise management of current generation in each individual sub cell is required to avoid current mismatch between the top cell and the bottom cell in monolithic two-terminal tandem structures. The compatibility of the fabrication processes for the top and bottom cells have to be considered as well. Monolithic three-terminal tandem systems can be also regarded as a parallel tandem, for which a mutual interlayer electrode with high electrical conductivity and good optical transparency is used to connect the sub cells with complementary absorption in parallel. This configuration allows the optimization of the current of each sub cell independently. However, compatibility of the fabrication processes during the monolithic growth is still needed. Mechanically stacked four-terminal tandem devices offer larger flexibility for different combinations of the top and bottom cells as the sub cells are mechanically stacked with independent connections between the top and bottom cells. Therefore, the issues of the current matching and the fabrication compatibility between the sub cells are not key concerns. While additional TCO electrodes involved in the four-terminal tandem devices will cause additional parasitic absorption, leading to current loss in the devices and thus the costs for materials, transportation and installation will increase due to the extra materials needed and the complexity of electrical connections. In the optical aspect, on the other hand, optical engineering such as different light trapping strategies can be employed to minimize the reflection losses at the various interfaces. Nevertheless, the four-terminal tandem architecture provides much more freedom for engineers to pair up the high-performance sub cells having complementary absorption spectra, facilitating the optimization of the module

transmissivity of each sub cell. For the case of perovskite/c-Si tandem devices, perovskite solar cells can be used as an add-on device putting on the top of commercial Si-based solar cells to further enhance the efficiency. It is noted that the semitransparent perovskite solar cell exhibits a PCE difference when it is illuminated from different sides of the electrodes due to the different transmittance of the electrodes and the parasitic absorption of the carrier transport layers (e.g. Spiro-MeOTAD). In the case of 4 terminal tandem devices, the side with larger transmission can be chosen as the illumination side. With proper integration of external circuit connections, four-terminal tandem devices can be effectively applied in practical applications such as the building-integrated photovoltaic (BIPV) system.

Previously, our group has successfully fabricated high performance single junction $CH_3NH_3PbI_3$ devices with PCE over 15% [32] for solution process and 17.6% for hybrid chemical vapor deposition process (HCVD) via careful controlling of the trap density in the bulk of the perovskite and material interfaces through post-deposition oxygen annealing treatment [32,33]. The next step to further boost the solar cell efficiency to a higher value desired for practical application is to combine the PSCs with c-Si solar cells in a tandem configuration. In this work, we report the development of high performance perovskite/c-Si four-terminal tandem devices accomplished by detailed material optimization and optical engineering of the devices. The strategy focuses on three aspects: (i) Enhancement of the transmissivity of the transparent rear electrode of the top cell; (ii) Passivation of defects in $CH_3NH_3PbI_3$ devices by post-deposition oxygen annealing; and (iii) Maximization of the light harvesting power of the tandem devices.

A number of techniques for preparing high transparency electrodes for perovskite top cells in tandem structures have been reported such as synthesis of silver nanowires [22], deposition of TCO by sputtering process [29, 30, 34], application of conducting multilayer [35], graphene [36] and poly(3,4,-ethylenedioxythiophene) (PEDOT:PSS) [37]. Among different techniques, the transmission spectra of multilayer electrodes can be easily tailored in accordance with the

absorption spectra of the absorbers used by adjusting the individual thickness of the constituent layers to increase the transparency of the electrode at certain wavelengths. A comprehensive investigation of optical and electrical properties of semi-transparent transition metal oxide/metal/ transition metal oxide multilayer electrode has been conducted in this work. The transparency of the transition metal oxide/metal/ transition metal oxide multilayer is then optimized based on the theoretical calculations specifically for the application in perovskite/c-Si four-terminal tandem solar cells.

Secondly, post-deposition oxygen treatment has been applied for achieving high performance MAM based perovskite devices. Both theoretical and experimental results show that oxygen is an essential element to reduce the localized states in the bulk of perovskite as well as at the material interfaces of the devices, yielding improved PV performance [32, 33, 38]. Furthermore, a light trapping strategy for increasing the effective optical paths passing through the absorber layer and thus enhancing the light harvesting power is incorporated into our perovskite/c-Si four-terminal tandem solar cells. It is demonstrated that a biomimicking elastomeric petal (BEP) replicated from natural rose petals can be used as versatile substrates for stretchable thin-film electronics. This is because the unique three-dimensional microscale crater-like topographies of the BEP prohibit the propagation of microcracks in the conducting films that are deposited on the elastomeric petal substrates during large-strain deformation [39]. It is recently discovered that such unique biological surface texture also behaves as an effective light scattering layer [40], exhibiting ultrahigh transmission haze of 75% and high diffusion transmittance of 97%. Therefore, the BEP can also be placed on the surface of the perovskite top cell to scatter the incident solar light to enhance the light harvesting power of the tandem structure. With the optimized optical properties for the device structure and careful defect engineering of the perovskite layer by low-temperature oxygen annealing, we have accomplished MAM-PSC with an average PCE of 16.6 %. The device is utilized to form a

tandem structure with a PCE 19.1% of c-Si cell and the tandem structure demonstrates an average PCE of 22.1%.

2. Materials and methods

2.1 Materials

Sylgard 184 polydimethylsiloxane (PDMS) pre-polymer and curing agent are purchased from Dow Corning. Titanium (IV) isopropoxide, lithium bis(trifluoromethylsulphonyl)imide (Li-TFSI), 4-tert-butylpyridine (tBP), N,N-dimethylformamide (DMF) and MoO_3 were supplied from Sigma-Aldrich while spiro-MeOTAD (purity> 99.5%) and Lead (II) chloride (purity 99%, $PbCl_2$) were purchased from Luminescence Technology Corp. Methylammonium iodide (CH_3NH_3I) was purchased from Dyesol. All chemicals were used as received.

2.2 BEP film fabrication

The BEP was prepared by replicating the surface texture of yellow rose petal by soft lithography. Briefly, PDMS pre-polymer (mixed with 10 wt% curing agent) was poured on the rose petal. The sample was then stored under vacuum to remove the air bubbles in the pre-polymer. After storing at room temperature for 2 days, the crosslinked PDMS was peeled off from the rose petal. Finally, the as-prepared PDMS film was cleaned by acetone and isopropanol under ultrasonification, and then cut into appropriate size to serve as BEP.

2.3 Perovskite solar cell fabrication

The perovskite films were deposited from a filtered saturated precursor solution containing 0.9 M $PbCl_2$ and CH_3NH_3I in DMF (1:3 molar ratio). The mixture solution was stirred at 75°C on the hotplate for 24 h, after that, a brightness yellow perovskite precursor solution was obtained by a 500 nm filter. Before spin-coating perovskite layer, the substrates and the perovskite precursor were preheated to 75°C and 90°C, respectively. The substrate was transferred quickly to the spin-coater, the precursor solution was deposited immediately afterward and the spin coater was started at 3000 rpm for 30 s. Subsequently, the substrate was annealed at 65°C for

15 min and 105°C for 45min. After the substrate cool down to the room temperature naturally, a hole transport layer was deposited by spin coating a solution of spiro-MeOTAD (80 mg/ml) dissolved in chlorobenzene with the additives of Li-TFSI (17.5 μL from a stock solution of 520 mg/ml in acetonitrile) and 29μL of tBP at 3000 rpm. The prepared samples were then placed in an oxidation furnace with a flow of O_2 at the rate of 2 lit/min at 65°C for 12 hours. The transparent electrode was prepared by thermal evaporation of MoO_3 and Au sequentially to form a MAM multilayer structure. The transmission and resistivity of the transparent MAM electrode were carefully optimized by adjusting the thickness of the constituent layers.

2.4 Silicon solar cell fabrication

For the fabrication of c-Si solar cells, boron-doped Cz-mono-Si wafers were used. The surface damage of Si wafers caused by cutting was eliminated by 20%wt KOH solution at 80°C. Random pyramid texture for light trapping of Si solar cell was achieved in mix solution of 5%wt KOH, IPA and additives at 80°C. After SiO_2 etched by HF solution, the wafers were loaded into a $POCl_3$ gas diffusion furnace for p-n junction formation with the diffusion temperature 830 °C for 20 min. The entire surface of the wafers was covered by phosphorus-doped layer (~70 ohm/sq). HF:HNO_3:H_2O (1:5:4) solution was used to etch the back junction. Passivation of the upper surface of the Si solar cell was achieved by ~80 nm of SiNx:H deposited by plasma-enhanced chemical vapor deposition (PECVD). Al_2O_3/SiN_x:H double layers passivation was adopted for the back surface of Si wafers. After laser opening the Al_2O_3/SiN_x:H layers with a certain pattern to expose part of the back surface of the Si wafers, the uniform Al paste and Ag paste were printed on the back and top surface of Si wafers by screen printing technology, respectively. The Al paste and Ag paste were co-fired with the peak temperature of 780°C.

2.5 Measurement and characterization

The *I-V* characteristics of devices were measured using a B1500A semiconductor parameter analyzer under the calibrated Oriel Sol3A solar simulator equipped with an AM 1.5 filter at 100 mW/cm^2 for top cell and a complete class AAA rated high-precision manual tester system (German Halm Cetis PV-Celltest3) for perovskite-filtered silicon solar cell, respectively. For top cell measurement, the light intensity was calibrated with a standard Si reference solar cell (Newport) and the light source was a 450 W xenon lamp (Oriel). The *J-V* curves in the main text were obtained from a double scan from 1.2 V to -0.2 V and -0.2 V to 1.2 V with a 20 mV scan step size. A stabilization time of 20 s at forward bias of 1.2 V was held prior to illumination and scanning. **Figure 6**a shows the *I-V* scan (forward and reverse direction) of the champion perovskite solar cell with and without BEP. The working area of the perovskite solar cell and silicon solar cell was 3 mm^2 and 120 mm^2, respectively. The EQE measurement was conducted by using solar cell spectral response measurement system (Model QEX10, America PV Measurements Inc.) with a 4 Hz chopping frequency, no extra bias illumination and voltage. As for the four-terminal tandem configuration in EQE measurement, the top perovskite cell is illuminated from the FTO side (with and without BEP) to the MAM electrode side and the bottom silicon solar cell is measured with an equivalent top perovskite device structure as the filter. The sheet resistances of MAM films were characterized by a four-probe test system. The transmittance spectra of MAM films were measured with LAMBDA 950 UV-Vis-NIR spectrometer from Perkin Elmer (England). TRPL signals were recorded using a time-correlated single photon counting (TCSPC) setup (Edinburgh FLSP920). Perovskite films were photoexcited using a 485 nm picosecond pulsed diode laser. The samples were exposed to pulsed light source for 10 minutes prior to measurement to enable stable sample emission. Time-resolved measurement was acquired from emission at 775 nm. For photothermal deflection spectroscopy measurement, the perovskite films were prepared on quartz substrate and immersed into FC-72, a monochromatic light beam, which was chopped at 13 Hz, was shined onto the sample and a laser was at the perpendicular side so that it was deflected

periodically. And the deflection signal was recorded by a position sensor, connected with a lock-in amplifier and placed on the other side. All measurements were conducted at ambient air condition and at room temperature.

3. Results and Discussion

The perovskite/c-Si four-terminal devices were fabricated based on the configuration as shown in **Figure** 1. It is noteworthy that this device architecture is not subject to current matching. Thus, we aim to optimize the PCE for each sub cell by maximizing the light harvesting power of the top PSC for short wavelengths with the aid of a novel light trapping technique and using highly transparent rear electrode for the top cell to ensure effective infrared photons absorption by c-Si bottom cell.

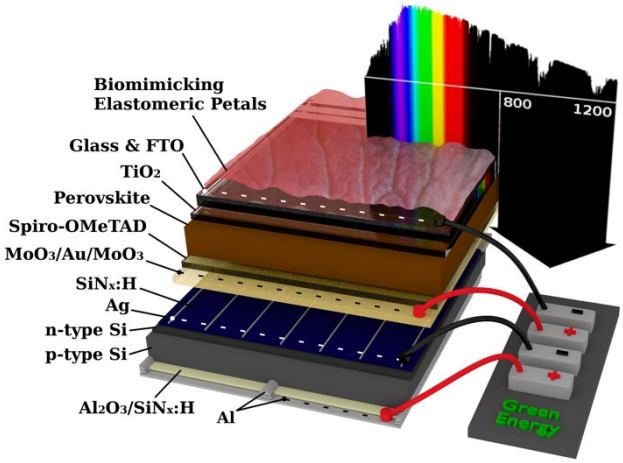

Figure 1. The device architecture of the four-terminal perovskite/c-Si tandem solar cell.

3.1 Peak Transmittance Tunable Metal Oxide/Metal/Metal Oxide Transparent Electrode

The transparent electrode consists of a thermally evaporated trilayer with an ultrathin Au film embedded between two layers of molybdenum trioxide (MoO_3). The electrical and optical properties of the MoO_3/Au/MoO_3 (MAM) electrode can be tuned by adjusting the thickness of the constituent layers. The first MoO_3 layer in contact with the spiro-MeOTAD is fixed at 15 nm which is in similar range of thickness used in the common metal oxide-metal-metal oxide electrode [41, 42]. The resistivity of the Au layer reduces with increasing thickness. However,

thick Au layer leads to poor transmissivity of the electrode as indicated in **Figure 2**a. Therefore, optimization of the transparency as well as the resistivity of the transparent MAM electrode is crucial to the overall performance of the device. The samples of MoO_3 (15 nm)/Au (*x* nm) were prepared and the sheet resistance of the samples with different thicknesses of Au were characterized. **Figure 2a** clearly shows the dependence of sheet resistance of the sample on the thickness of Au. It is found that the value of the sheet resistance drops significantly from ~460 ohm/sq to ~40 ohm/sq when the thickness of Au increases from 6 nm to 10 nm. The sheet resistance further reduces to 15 ohm/sq when the Au layer increases to 12 nm while further increase of Au thickness does not lead to obvious reduction in sheet resistance. In order to achieve high transmissivity as well as good conductivity of the transparent MAM electrode, the thickness of Au was fixed at 12 nm, then, the thickness of the MoO_3 capping layer was varied and the sheet resistance of the layer underneath was recorded was shown in **Figure 2**b.

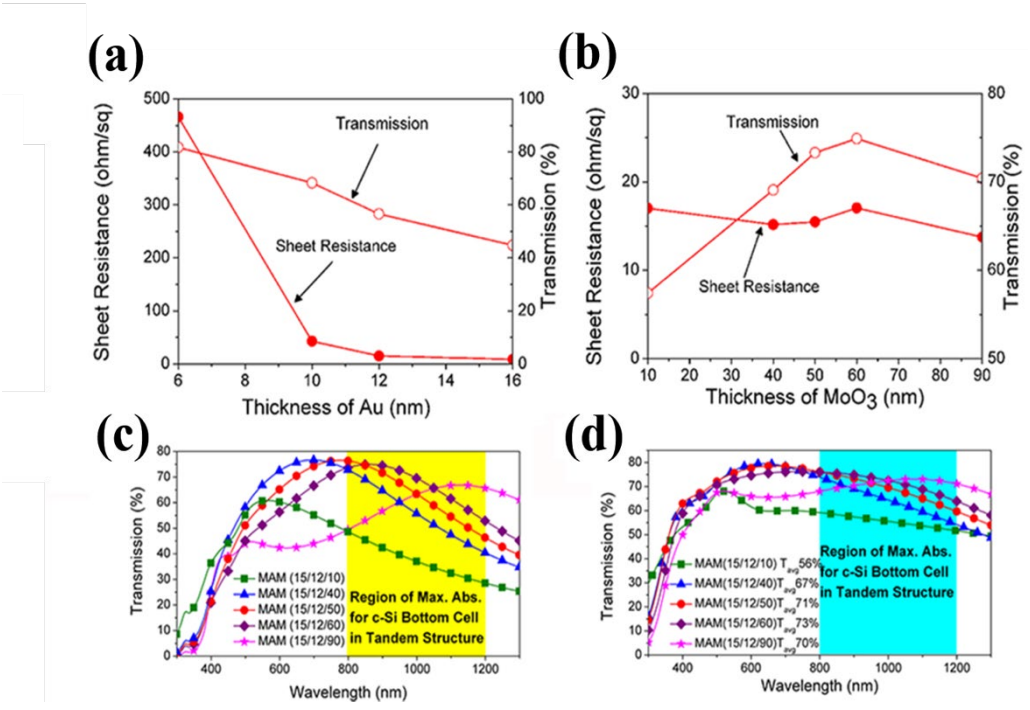

Figure 2. The experimental data for the sheet resistance and transmission of a) MoO_3 (15 nm)/Au (*x* nm); b) the experimental data for the sheet resistance and transmission at 900 nm of MoO_3 (15 nm)/Au (12 nm)/MoO_3 (*x* nm); c) the simulated transmission data for MAM electrode

with different thickness of capping MoO_3 layer and d) the experimental transmission data for MAM electrode with different thickness of MoO_3 capping layer (The average values of transmission from 800 nm to 1200 nm are also indicated).

It is found that the thickness of the MoO_3 capping layer does not affect the sheet resistance of its underlying MoO_3/Au layer. However, calculated results in **Figure 2**c show that the MAM electrode with different thickness of the MoO_3 capping layer strongly affects the peak position of the transmission spectrum of the electrode which was also characterized experimentally as shown in **Figure 2**d. Therefore, the peak transmittance of MAM layer can be precisely tuned from visible to near infrared by changing the thickness of the last MoO_3 capping layer. It is noted that the transmission peaks of the experimental results are generally consistent with the simulated results. The primary difference between the simulated and experimental results is the amplitudes, which is possibly due to the difference in the index of refraction of the materials used in the simulation and experiment. The index of refraction of the materials supplied from different sources and prepared in different condition of the deposition chamber will be slightly different. For the four-terminal tandem device, the MAM electrode has to be highly transparent at the long wavelength range for the infrared photons to enter the bottom silicon layer located below the top PSC. Therefore, the transmission of the MAM electrode at long wavelengths, particularly between 800 nm to 1200 nm, should be maximized. Our experimental results in **Figure 2**d show that the MoO_3 (15 nm)/Au (12 nm)/MoO_3 (60 nm) trilayer exhibits the highest average transmission of ~73 % between 800 nm and 1200 nm compared to other combinations, which agree with the simulation results shown in **Figure 2**c. It is noteworthy that the sheet resistance of the MAM electrode prepared by the proposed method is an order of magnitude lower compared to the common transparent graphene electrode with similar transmission [36]. The conventional TCOs such as ITO, FTO and AZO generally have higher transparency. However, their film deposition usually involves high energetic processes (sputtering, e-beam),

which will easily damage the perovskite film and degrade the performance of the device. To minimize the negative impact, a buffer layer will be prepared on the sample prior to the TCO deposition. The conductivity of these TCOs strongly depends on a number of deposition parameters such as substrate temperatures, types of ambient gases and flow rate of the gases etc. In this work, the MAM electrode prepared by thermal evaporation, which is a relatively mild deposition process provides an alternative for the device with the delicate constituent layers. The conductivity of MAM mainly depends on the thickness of MoO_3 and Au, which involve relatively less parameters needed to be controlled. The transmission spectrum of MAM multilayers can also be modified by changing the thickness of the MoO_3 capping layer. The peak transmission of MAM can be tuned in order to maximize the transparency of the electrode to the long-wavelength photons for the bottom c-Si cell. The application of MAM as the transparent electrode has significant advantages for future large-scale industrial fabrication as the deposition process can be precisely controlled by the evaporation system with an accurate thickness monitor. The inset digital image in **Figure 3**a shows the color of the MAM electrodes with different thicknesses of MoO_3 capping layer deposited on the quartz. Different degree of transparencies of the MAM trilayers can be observed with the naked eye by varying the thickness of MoO_3 capping layer. We then fabricate the PSCs using the optimized transparent MAM (15 nm/12 nm/60 nm) electrode. The transmission spectra of the samples with different incremental layer stack structures are shown in **Figure 3b**. The transmission for the sample with the complete perovskite device structure is ~50 % at long wavelengths. Further enhancement of the transmission of the top PSC can be achieved if larger band gap perovskite materials and hole transport materials with lower absorption are used. The cross-sectional image of the device with MAM electrode is shown in **Figure 3a**. The thicknesses for perovskite absorber and spiro-MeOTAD layers are around 350 nm and 200 nm respectively. **Figure 3c and 3d** shows the image of the topography of the MAM electrode obtained from the atomic

force microscopy. The RMS roughness of the sample MoO_3 (15 nm)/Au (12nm) is 1.08 nm while the value reduces to 0.54 nm after depositing 60 nm MoO_3 capping layer.

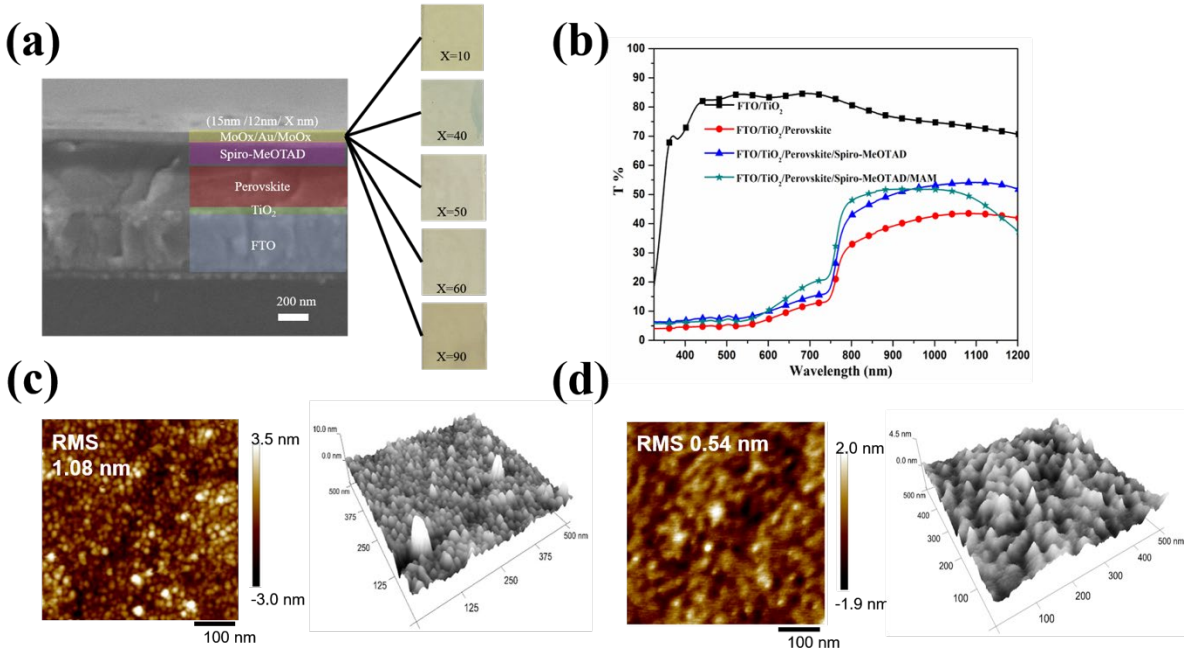

Figure 3. (a) Cross sectional SEM image of the perovskite device with MAM electrode. Inset: the photograph of the MAM electrode with different thickness of MoO_3 capping layer deposited on quartz (the thickness of each layer is indicated in the bracket in form of MoO3/Au/MoO3 unit: nm). (b) The transmission spectra of MAM based perovskite solar cell with different incremental layer stack structures: FTO/TiO_2 layer (square), FTO/TiO_2/Perovskite stack layer (circle), FTO/TiO_2/Perovskite/Spiro-MeOTAD stack layer (triangle), and the whole perovskite solar cell stack layer (star). The AFM topography image for (c) MoO_3 (15 nm)/Au (12nm) layer (roughness (RMS): 1.08 nm) and (d) MoO_3 (15 nm)/Au (12nm)/ MoO_3 (60 nm) layer (roughness (RMS): 0.54 nm)

3.2 Oxygen post-deposition treatment

Oxygen post-deposition treatment is applied for the PSCs before the electrode deposition for enhancing the PCE. The comparisons of the PV parameters between the devices with or without oxygen post-deposition treatment are shown in **Table 1**. It is observed that the

performance of the PSC is highly sensitive to the oxygen post-deposition treatment. The V_{OC}, short circuit current density (J_{SC}) and fill factor (FF) of the devices are dramatically improved after oxygen post-deposition treatment. An average PCE of 17.3 % for the PSCs with oxygen post-deposition treatment can be obtained compared to the average PCE of 14.6% for the control devices without the oxygen post-deposition treatment. The typical steady-state current density and PCE measured at the maximum power point for the optimized device are shown in **Figure 4**a. A stable output with the stabilized PCE of 17.2 % is obtained for the device, which is in excellent agreement with the results of the *I-V* measurement as shown in **Table 1**. The substantial reduction in the trap density of the perovskite material is the major reason for the enhancement in device performance. The spectra of photothermal deflection spectroscopy (PDS) for the perovskite films deposited on quartz with and without oxygen post-deposition treatment are shown in **Figure 4**b.

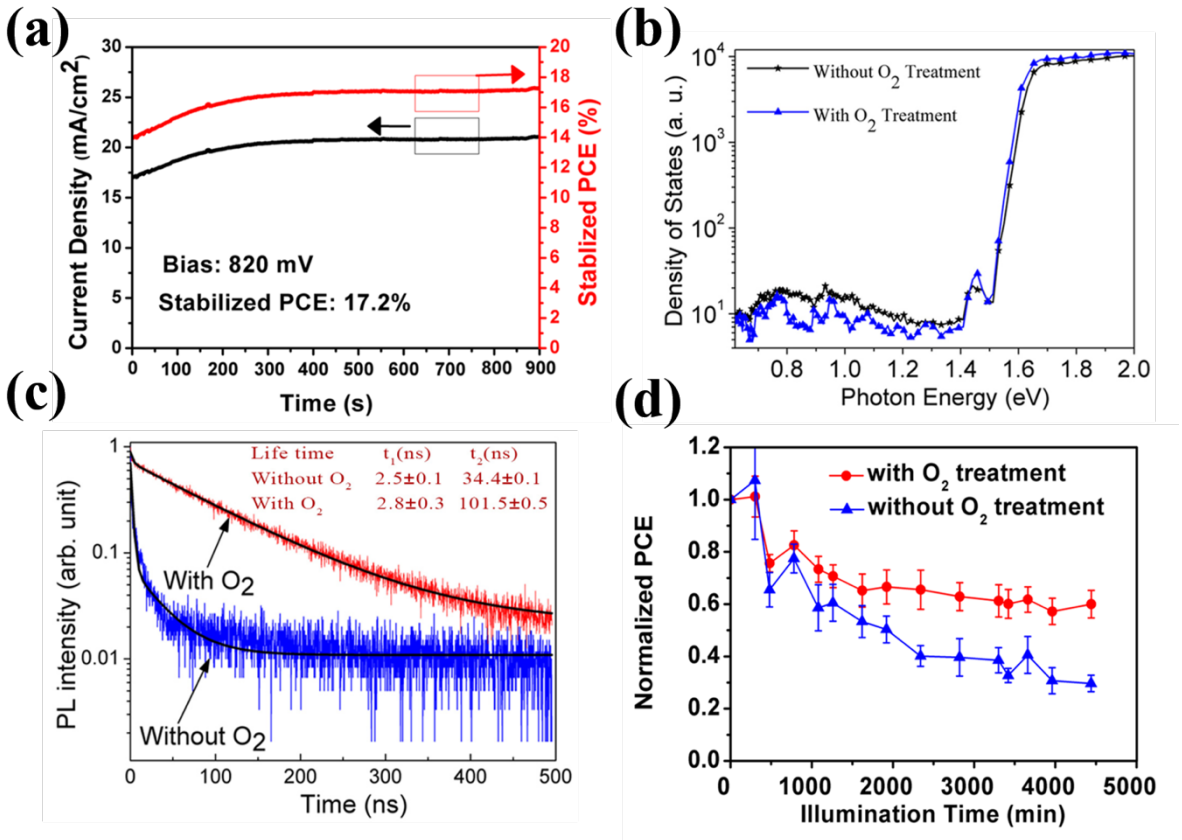

Figure 4. (a) The steady-state current density and PCE measured at the maximum power point for the device with oxygen annealing. The results obtained from (b) the photothermal deflection spectroscopy and (c) TRPL for the perovskite films with and without oxygen treatment. (d) The degradation of the devices (average of 8 devices) with and without oxygen annealing under 1 sun illumination.

The technique of PDS is commonly used to characterize the energetic disorder as the exponential decay of the absorption below the bandgap with a characteristic Urbach energy. The Urbach energies, determined from the PDS spectra are 20.1 meV for the control sample and 18.9 meV for the sample with oxygen post-deposition treatment. The smaller Urbach energy and lower sub-bandgap absorption for the sample with oxygen treatment clearly indicate that the introduction of oxygen is able to reduce the density of bandgap states in the perovskite layer. Time-resolved photoluminescence (TRPL) signals were recorded for perovskite films with and without oxygen treatment. The experimental results are shown in **Figure 4**c. The data are fitted with the bi-exponential decay function, in which two individual lifetimes can be extracted from the decay curves. Substantial enhancements in the carrier lifetimes from t_1=2.5 ns and t_2= 34.4 ns to t_1=2.8 ns and t_2= 101.5 ns are observed for the perovskite sample after oxygen post-deposition treatment. It is attributed to the passivation of the traps in the perovskite during oxygen post-deposition process and hence reduces the chance of carrier recombination, leading to longer carrier lifetimes. The TRPL results are highly consistent with the PDS data. In accordance to the previously reported PL decay of the perovskite films [1-3], the fast decay component t_1 could be attributed to bimolecular recombination [4] and the long decay component t_2 come from the recombination of free carriers in the radiative channel [5].

Apart from the high efficiency of the devices, device stability is also an important criterion for future commercialization. Some initial works of device stability under illumination have been conducted. The results show that the degradation rate of the encapsulated devices with

oxygen post-deposition treatment under 1 sun illumination is substantially smaller compared to the devices without oxygen post-deposition treatment as shown in the **Figure 4**d. It is indicated that oxygen post-deposition treatment also has positive impact on the lifetime of the perovskite devices due to the reduction of the trap density of the perovskite materials. It is believed that the mechanism of the device degradation is complicated, which can be mutually affected by a number of material and environmental factors. Further investigations on the device lifetime are in progress.

Table 1. The comparison of perovskite devices with and without post-deposition oxygen annealing. (i. Devices without O_2 annealing. ii. Devices with O_2 annealing)

Device	Results	V_{OC} (V)	J_{SC} (mA/cm^2)	FF（%）	PCE (%)
(i)	Average (8 devices)	1.03 ± 0.02	20.1 ± 0.7	0.70 ± 0.02	14.6 ± 0.9
	Best	1.06	21.4	0.69	15.7
(ii)	Average (8 devices)	1.07 ± 0.01	22.0 ± 1.0	0.73 ± 0.01	17.3 ± 0.7
	Best	1.07	23.6	0.72	18.1

3.3 Biomimicking Elastomeric Petals Light Trapping Film

A BEP is applied at the top of the PSC for more efficient light absorption. The BEP is fabricated by replicating the surface texture of rose petal with PDMS through soft lithography. The morphology and mechanism of the BEP are shown in the **Figure 5**. The SEM top view of the BEP is presented in **Figure 5**a (Inset is the digital image of rose petal mold and the PDMS BEP film) and its 3D morphology (**Figure 5**b) is also simulated and demonstrated by the professional image-process software. It is found that the simulated 3D regular microstructures, replicated from the surface texture of rose petal, are similar to micro-lens array. These regular micro structures serve as mirco-lens array, which scatters the incident light and thus lengthens the optical path of the active material underneath (**Figure 5**c and **Figure 5**d).

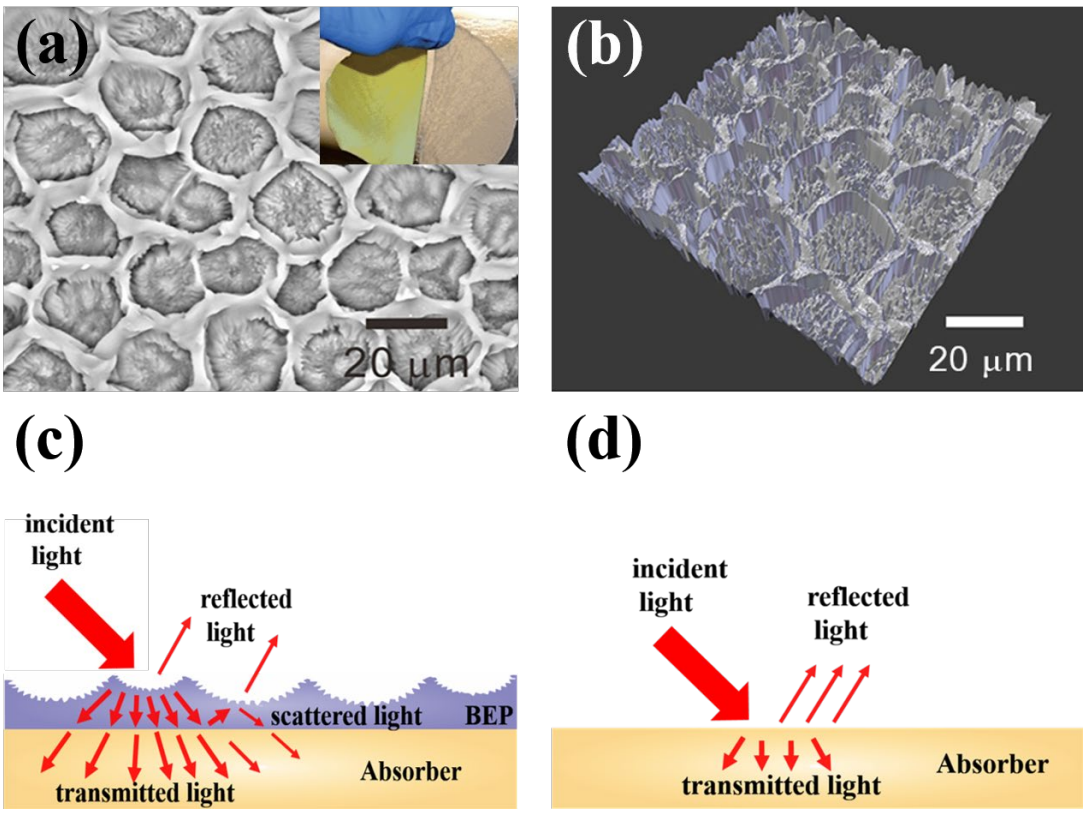

Figure 5. (a) The SEM top view of the biomimicking elastomeric petals. Inset is the digital image of rose petal mold and the PDMS BEP film. (b) 3D morphology simulated model of the SEM top view. (c) the optical paths for the substrate with light trapping layer and (d) the optical paths for the substrate without light trapping layer.

3.4 Perovskite/Crystalline Silicon Four-Terminal Tandem Solar Cells

The BEP significantly improves the J_{SC} of the PSC and hence substantial improvement in PCE can be achieved. The average PV parameters are summarized in the Table S1. With the application of the light trapping layer, the J_{SC} and PCE of a typical MAM transparent device are increased from 22.4 mA/cm^2 to 23.7 mA/cm^2 and from 16.7 % to 17.9 % (reverse scan) as demonstrated in Table 2. It is noted that the BEP causes marginal reduction in PCE (0.3 %) for the c-Si bottom cell in the tandem system while significantly enhances the efficiency of the top PSC, because the scattering effect of the BEP reduces the total number of the photons passing through the semi-transparent top PSC. Since the PCE enhancement in the top PSC outweighs

the PCE reduction in the bottom c-Si cell, it is clear that the overall performance of the perovskite/c-Si tandem solar cell can be significantly improved by application of the BEP. The impact of the BEP films on different types photovoltaic and their optical properties have been comprehensively discussed in our paper which has been published during the reviewing process of this work. The hysteresis effect of the *I-V* measurement is observed for our planar PSCs. The *J-V* curves for forward and reverse scan of the perovskite top cell with and without light trapping are shown in **Figure 6a**. There is little hysteresis for the reverse and forward scan and it is believed that further enhancement in charge extraction efficiency by optimizing the material interfaces, particularly for the TiO_2/perovskite interface can minimize the hysteresis effect in the perovskite device [43].

Table 2. The typical photovoltaic parameters of different type of solar cells with or without light trapping layer. (i. c-Si; ii. c-Si filtered without light trapping; iii. c-Si filtered with light trapping; iv. Semi-transparent perovskite; v. Semi-transparent perovskite with light trapping; vi. Perovskite/c-Si tandem with light trapping)

Sample		V_{OC} (V)	J_{SC} (mA/cm^2)	FF (%)	PCE (%)	$PCE_{average}$ (%)
(i)		0.63	40.2	0.75	19.1	-
(ii)		0.59	13.0	0.75	5.8	-
(iii)		0.59	12.5	0.75	5.5	-
(iv)	Reverse	1.03	22.4	0.73	16.7	16.0
	Forward	0.97	22.4	0.70	15.3	
(v)	Reverse	1.06	23.7	0.71	17.9	16.6
	Forward	0.99	23.7	0.67	15.3	
(vi)		-				22.1

The top PSC and the bottom c-Si cell are integrated in proper electric connection as shown in **Figure S1**. The corresponding *I-V* characteristics and EQE results are summarized in **Figure 6**. The tandem device without light trapping technique yields an average PCE of 21.8%, compared to 16.7% and 19.1% for the PSC and c-Si solar cell operated individually. After incorporating the BEP as the light trapping layer, the performance of the tandem device can be significantly enhanced to an average PCE of 22.1 % as shown in the Table 2. It is noted that

there is 7.6% and 10.5% discrepancy between the integrated J_{SC} from the EQE results and the J_{SC} obtained from the *I-V* measurement for the PSC without and with the BEP. The underestimation of EQE sometimes happens in PSCs. This phenomenon can be attributed to the barrier for the photocurrent of MAM-PSC which becomes dominant under momochromatic illumination with low light intensity during EQE measurement while the barrier will be alleviated by photodoping of the perovskite under the 1 sun illumination [44]. It is also found that the light trapping effect of the BEP on the PSCs under the EQE measuring conditions is relatively not as effective as the PSCs for the *I-V* scan under the 1 sun solar simulator. The light trapping power is more substantial when the PSCs are illuminated by a light source (1 sun solar simulator), which is significantly larger than the device area. The spot size in the EQE measurement is smaller than the tested devices, which will diminish the light scattering effect as the unique pattern of biomimicking elastomeric petals performs stronger light tripping power in a larger illumination area.

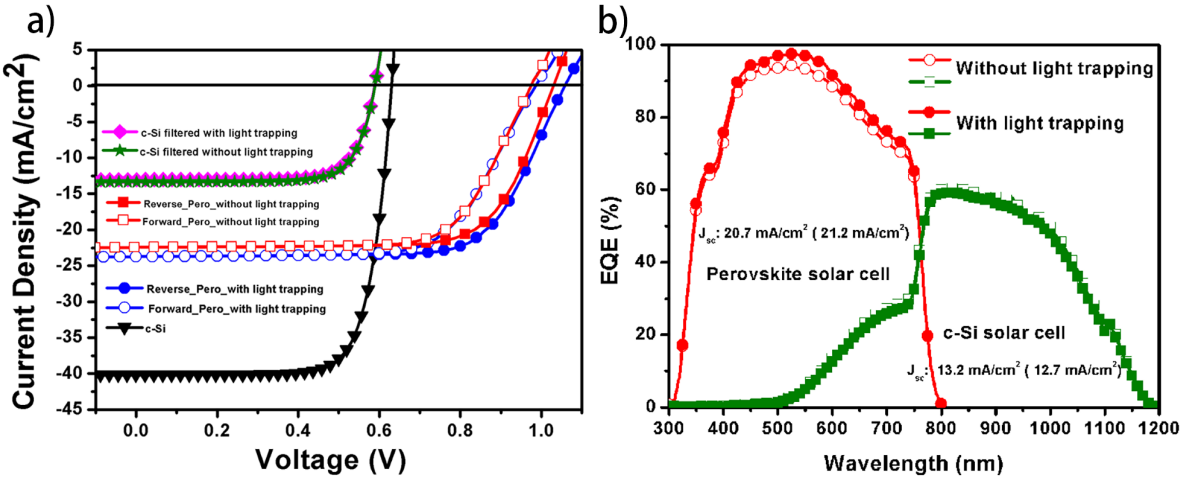

Figure 6. a) The *I-V* characteristics of the c-Si solar cell with and without perovskite filter and perovskite solar cell with and without light trapping. b) The EQE of the perovskite solar cell and filtered c-Si solar cell with and without light trapping (integrated J_{SC} for c-Si, c-Si with light trapping, perovskite, perovskite with light trapping are 13.2 mA/cm^2, 12.7 mA/cm^2, 20.7 mA/cm^2 and 21.2 mA/cm^2).

4. Conclusion

We successfully demonstrate the high efficiency perovskite/c-Si solar cells by incorporating high quality transparent MAM electrode for perovskite top cell, reducing trap density of perovskite films by oxygen post-deposition treatment and applying effective BEP as the light trapping layer. It is found that the resistivity of the MAM multilayer electrode can be controlled by the thickness of Au while the transmission peak of the electrode can be obtained at long wavelengths by varying the thickness the MoO_3 capping layer, which is an effective strategy for maximizing the light passing from the perovskite top cell to the bottom c-Si sub cell. The BEP attached on the light incident surface of the tandem device can dramatically enhance the optical paths by the scattering effect and hence improve the light harvesting power of the tandem structure. An average PCE of 22.1 % was obtained for the perovskite/c-Si four-terminal tandem device with optimized optical features. The proposed tandem devices can be used in the future practical applications such as development of the building-integrated photovoltaic (BIPV) system.

Acknowledgements
This work was supported by the RGC Theme-based Research Scheme (Grant number: HKU T23-713/11), ECS of Hong Kong (PolyU 5030/12P), GRF of Hong Kong (PolyU 5036/13P), The Hong Kong Polytechnic University (Project 1-ZVGH, 1-ZVK1), the Clarea Au Endowment Professorship and Central Research Grant of The Hong Kong Polytechnic University, and the Guangdong-Hong Kong Technology Cooperation Funding Scheme (2014B050505010).

Received: ((will be filled in by the editorial staff))
Revised: ((will be filled in by the editorial staff))
Published online: ((will be filled in by the editorial staff))

Appendix A. Supplementary material
Supplementary data associated with this article can be found in the online version

References

[1] D. Bi, W. Tress, M. I. Dar, P. Gao, J. Luo, C. Renevier, K. Schenk, A. Abate, F. Giordano, J.-P. C. Baena, Sci. Adv. 2 (2016) e1501170.

[2] W. S. Yang, J. H. Noh, N. J. Jeon, Y. C. Kim, S. Ryu, J. Seo, S. I. Seok, Science 348 (2015) 1234-1237.

[3] G. Niu, X. Guo, L. Wang, J. Mater. Chem. A 3 (2015) 8970-8980.

[4] A. Djurišić, F. Liu, A. Ng, Q. Dong, M. K. Wong, A. Ng, C. Surya, Phys. Status Solidi 4 (2017) 273-354.

[5] F. Liu, Q. Dong, M. K. Wong, A. B. Djurišić, A. Ng, Z. Ren, Q. Shen, C. Surya, W. K. Chan, J. Wang, Adv. Energ. Mater. 6 (2016)1502206.

[6] A. Kojima, K. Teshima, Y. Shirai, T. Miyasaka, J. Am. Chem. Soc. 131 (2009) 6050-6051.

[7] H.-S. Kim, C.-R. Lee, J.-H. Im, K.-B. Lee, T. Moehl, A. Marchioro, S.-J. Moon, R. Humphry-Baker, J.-H. Yum, J. E. Moser, Sci. Rep. 2 (2012) 591.

[8] National Renewable Energy Laboratory, Research Cell Record Efficiency Chart, http://www.nrel.gov/pv/assets/images/efficiency-chart.png, accessed: Jan, 2017.

[9] G. E. Eperon, S. D. Stranks, C. Menelaou, M. B. Johnston, L. M. Herz, H. J. Snaith, Energ. Environ. Sci. 7 (2014) 982-988.

[10] J.-H. Im, C.-R. Lee, J.-W. Lee, S.-W. Park, N.-G. Park, Nanoscale 3 (2011) 4088-4093.

[11] S. D. Stranks, G. E. Eperon, G. Grancini, C. Menelaou, M. J. Alcocer, T. Leijtens, L. M. Herz, A. Petrozza, H. J. Snaith, Science 342 (2013) 341-344.

[12] G. Xing, N. Mathews, S. Sun, S. S. Lim, Y. M. Lam, M. Grätzel, S. Mhaisalkar, T. C. Sum, Science 342 (2013) 344-347.

[13] M. M. Lee, J. Teuscher, T. Miyasaka, T. N. Murakami, H. J. Snaith, Science 338 (2012) 643-647.

[14] C. C. Stoumpos, C. D. Malliakas, M. G. Kanatzidis, Inorg. Chem. 52 (2013) 9019-9038.

[15] G. Hodes, Science 342 (2013) 317-318.

[16] D. B. Mitzi, Prog. Inorg. Chem., 48 (2007)1-121.

[17] Best Research Cell Efficiency, NREL, https://www.nrel.gov/pv/assets/images/efficiency-chart.png, accessed Dec 2017.

[18] A. Richter, M. Hermle, S. W. Glunz, IEEE J. Photovolt. 3 (2013) 1184-1191.

[19] S. Essig, J. Benick, M. Schachtner, A. Wekkeli, M. Hermle, F. Dimroth, IEEE J. Photovolt. 5 (2015) 977-981.

[20] S. Essig, S. Ward, M. A. Steiner, D. J. Friedman, J. F. Geisz,; P. Stradins, D. L. Young, Energy Procedia 77 (2015) 464-469.

[21] B. Chen, Y. Bai, Z. Yu, T. Li, X. Zheng, Q. Dong, L. Shen, M. Boccard, A. Gruverman, Z. Holman, J. Huang, Adv. Energy Mater. 6 (2016) 1601128.

[22] C. D. Bailie, M. G. Christoforo, J. P. Mailoa, A. R. Bowring, E. L. Unger, W. H. Nguyen, J. Burschka, N. Pellet, J. Z. Lee, M. Grätzel, Energ. Environ. Sci. 8 (2015) 956-963.

[23] S. Albrecht, M. Saliba, J. P. C. Baena, F. Lang, L. Kegelmann, M. Mews, L. Steier A. Abate, J. Rappich, L. Korte, R. Schlatmann, M. K. Nazeeruddin, A. Hagfeldt, M. Grätzel, B. Rech, Energy Environ. Sci. 9 (2016) 81-88.

[24] J. Werner, C.-H. Weng, A. Walter, L. Fesquet, J. P. Seif, S. D. Wolf, B. Niesen, C. Ballif, J. Phys. Chem. Lett. 7 (2016) 161-166.

[25] L. Dou, J. You, J. Yang, C.-C. Chen, Y. He, S. Murase, T. Moriarty, K. Emery, G. Li, Y. Yang, Nat. Photonics 6 (2012) 180-185.

[26] J. You, L. Dou, K. Yoshimura, T. Kato, K. Ohya, T. Moriarty, K. Emery, C.-C. Chen, J. Gao, G. Li, Nat. Commun. 4 (2013) 1446.

[27] S. Tanaka, K. Mielczarek, R. Ovalle- Robles, B. Wang, D. Hsu, A. Zakhidov, Appl. Phys. Lett. 94 (2009) 113506.

[28] X. Guo, F. Liu, W. Yue, Z. Xie, Y. Geng, L. Wang, Org. Electron. 10 (2009) 1174-1177.

[29] P. Löper, S.-J. Moon, S. M. De Nicolas, B. Niesen, M. Ledinsky, S. Nicolay, J. Bailat, J.-H. Yum, S. De Wolf, C. Ballif, Phys. Chem. Chem. Phys. 17 (2015) 1619-1629.

[30] J. Werner, G. Dubuis, A. Walter, P. Löper, S.-J. Moon, S. Nicolay, M. Morales-Masis, S. De Wolf, B. Niesen, C. Ballif, Sol. Energ. Mat. Sol. 141 (2015) 407-413.

[31] P. Kumar, S. Chand, Prog. Photovolt: Res. Appl. 20 (2012) 377-415.

[32] Z. Ren, A. Ng, Q. Shen, H. C. Gokkaya, J. Wang, L. Yang, W.-K. Yiu, G. Bai, A. B. Djurišić, W. W.-F. Leung, Sci. Rep. 4 (2014) 6752.

[33] A. Ng, Z. Ren, Q. Shen, S. H. Cheung, H. C. Gokkaya, G. Bai, J. Wang, L. Yang, S. K. So, A. B. Djurišić, J. Mater. Chem. A 3 (2015) 9223-9231.

[34] F. Fu, T. Feurer, T. Jäger, E. Avancini, B. Bissig, S. Yoon, S. Buecheler, A. N. Tiwari, Nat. Commun. 6 (2015) 8932.

[35] J. Liu, S. Lu, L. Zhu, X. Li, W. C. Choy, Nanoscale 8 (2016) 3638-3646.

[36] F. Lang, M. A. Gluba, S. Albrecht, J. r. Rappich, L. Korte, B. Rech, N. H. Nickel, J. Phys. Chem. Lett. 6 (2015) 2745-2750.

[37] Y. Xiao, G. Han, J. Wu, J.-Y. Lin, J. Power Sources 306 (2016) 171-177.

[38] W. J. Yin, H. Chen, T. Shi, S. H. Wei, Y. Yan, Adv. Electron. Mater. 1 (2015) 1500044.

[39] R. Guo, Y. Yu, J. Zeng, X. Liu, X. Zhou, L. Niu, T. Gao, K. Li, Y. Yang, F. Zhou, Adv. Sci. 2 (2015)1400021.

[40] K. Li, Y. Zhang, H. Zhen, H. Wang, S. Liu, F. Yan, Z. Zheng, J. Mater. Chem. A. 5 (2017) 969.

[41] D. Sahu, S.-Y. Lin, J.-L. Huang, Appl. Surf. Sci. 252 (2006) 7509-7514.

[42] T. Winkler, H. Schmidt, H. Flügge, F. Nikolayzik, I. Baumann, S. Schmale, T. Weimann, P. Hinze, H.-H. Johannes, T. Rabe, Org. Electron. 12 (2011) 1612-1618.

[43] S. D. Stranks, H. J. Snaith, Nat. Nanotech. 10 (2015) 391-402.

[44] R. Scheer, H.-W. Schock, John Wiley & Sons: 7 (2011) 305-315.

Keyword: tandem solar cells, perovskites, silicon, transparent electrodes, oxygen annealing, biomimicking elastomeric petals